

Research Article

A Photoelectric-Stimulated MoS₂ Transistor for Neuromorphic Engineering

Shuiyuan Wang,¹ Xiang Hou,¹ Lan Liu,¹ Jingyu Li,¹ Yuwei Shan,² Shiwei Wu,²
David Wei Zhang,¹ and Peng Zhou¹

¹ASIC & System State Key Lab., School of Microelectronics, Fudan University, Shanghai 200433, China

²Department of Physics, State Key Laboratory of Surface Physics, Key Laboratory of Micro and Nano Photonic Structures (Ministry of Education), and Institute for Nanoelectronic Devices and Quantum Computing, Fudan University, Shanghai 200433, China

Correspondence should be addressed to Peng Zhou; pengzhou@fudan.edu.cn

Received 23 June 2019; Accepted 14 October 2019; Published 11 November 2019

Copyright © 2019 Shuiyuan Wang et al. Exclusive Licensee Science and Technology Review Publishing House. Distributed under a Creative Commons Attribution License (CC BY 4.0).

The von Neumann bottleneck has spawned the rapid expansion of neuromorphic engineering and brain-like networks. Synapses serve as bridges for information transmission and connection in the biological nervous system. The direct implementation of neural networks may depend on novel materials and devices that mimic natural neuronal and synaptic behavior. By exploiting the interfacial effects between MoS₂ and AlO_x, we demonstrate that an h-BN-encapsulated MoS₂ artificial synapse transistor can mimic the basic synaptic behaviors, including EPSC, PPF, LTP, and LTD. Efficient optoelectronic spikes enable simulation of synaptic gain, frequency, and weight plasticity. The Pavlov classical conditioning experiment was successfully simulated by electrical tuning, showing associated learning behavior. In addition, h-BN encapsulation effectively improves the environmental time stability of our devices. Our h-BN-encapsulated MoS₂ artificial synapse provides a new paradigm for hardware implementation of neuromorphic engineering.

1. Introduction

The challenges of traditional computing architectures stem from storage capacity limitations and the high cost of specific data transfer speeds between memory and processors, the so-called von Neumann bottleneck [1–5]. With the advent of the artificial intelligence and big data era, this dilemma is becoming more profound. Brain-inspired neuromorphic engineering is different to the von Neumann architecture, combining memory and computation, with efficient energy utilization, and flexible adaptive and massively parallel computing capabilities [6]. It may achieve unprecedented technological breakthroughs, fundamentally overcoming the von Neumann bottleneck [7, 8]. Artificial synapses, just as those in the biological nervous system [9], play an important role in connecting various neuron blocks as the basic units of neuromorphic engineering [10]. Constructing new, stable, reliable, and efficient artificial high-performance synaptic devices is essential for neuromorphic engineering and neural network computing

[11]. Many artificial synaptic devices have been reported, including oxide electric double layer [12–14], ionic liquid/gel transistors [15–20], memristors [21–29], phase-changed memory [30–34], and ferroelectric transistors [35–37]. Also, the unique internal and interfacial structures of two-dimensional (2D) materials, as well as their electrical and optical properties [38–40], make them promising candidates for complex neuromorphic engineering [41–45]. In addition, optical modulation can establish a connection between the external environment and the brain through the visual system [46–48], and combining effective optoelectronic modulation is critical for neuromorphic engineering applications, such as artificial eyes and super vision [49–51].

Here, we demonstrate an efficient photoelectrical tunable h-BN-encapsulated MoS₂ synaptic transistor with basic synaptic functions. Furthermore, under electrical modulation, we successfully simulate the impressive Pavlov classical conditioning experiment through V_{bg} tuning, which realizes the acquisition, extinction, and recovery function of associated

learning. Due to the h-BN encapsulation, our devices exhibit superior environmental time stability. Our h-BN-encapsulated MoS₂ artificial synaptic transistor provides a novel paradigm for neuromorphic engineering based on 2D materials.

2. Results

First, we fabricated an h-BN-encapsulated MoS₂ synaptic transistor on an AlO_x/Si substrate, which simulates synaptic behavior by photoelectric stimulation, as shown in Figures 1(a) and 1(b). 2D layered h-BN and MoS₂ were prepared by mechanical exfoliating. The surface morphology of our device was characterized by scanning electron microscopy (SEM) and atomic force microscopy (AFM), as shown in Figure 1(c) and Figure S2a, respectively, showing a typical channel width of 10 μm, a length of 15 μm, and the thickness of the MoS₂; h-BN was approximately 1.7 and 7 nm. The Raman spectrum shows the characteristic peaks of both materials: Raman shift of the MoS₂ characteristic peak is 385,405 cm⁻¹ (Figure 1(e)) and the h-BN is 1366 cm⁻¹ (Figure S2b), which is consistent with previous reports. Figure 1(d) shows the Raman mapping of h-BN-encapsulated MoS₂ synaptic transistor at 405 cm⁻¹, the channel MoS₂ exhibits intense intensity, and the h-BN/MoS₂ overlap region is more strongly correlated with h-BN encapsulation, where the black and gray dashed areas represent the h-BN/MoS₂ overlap region and channel MoS₂, respectively. A significant peak was observed in the PL spectrum of MoS₂ at 1.88 eV photon energy (Figure 1(f)), which is consistent with the band gap of multilayer MoS₂. Then, we studied the behavioral characteristics of our h-BN-encapsulated MoS₂ synaptic transistor under electrical modulation. Figure 2(a) shows the I_{ds} - V_{bg} curves of the h-BN-encapsulated MoS₂ synaptic transistor with V_{ds} of 0.1, 0.5, and 1 V. The back gate voltage was swept from -6 to 8 V, then swept back, and a noticeable clockwise hysteresis loop was observed, which may be due to charge trapping between the MoS₂ and AlO_x interfaces. The statistical distribution of the maximum value of the memory window indicates that the memory window of most devices is 2~3 V (see the statistics of 80 devices in Figure S11a in Supplementary Materials). The transfer curves of the h-BN/MoS₂/h-BN control devices show no hysteresis window, since the bottom h-BN isolates the interface effect of MoS₂ and AlO_x (see Figures S10a-c, the schematic diagram of the control devices, micrograph of the control device, and transfer curves of the control devices in Supplementary Materials). Owing to top encapsulated h-BN, the stability of our devices has been significantly improved (see Figure S3, output curves and stability of h-BN-encapsulated MoS₂ synaptic transistor in Supplementary Materials) [52–55]. We explored the optimal base and pulse voltages for device operation in electrical mode for excitatory and inhibitory synapses, with reference to gain (A_2/A_1 , the amplitude of the postsynaptic current caused by spike is denoted by A) of five consecutive pulses and long-term synaptic weight changes ($\Delta W/W$, calculated by $(I - I_0)/I_0 * 100%$, where I_0 and I represent the current states before and after the application of the

pulse signal, respectively. Before applying the pulse signal, we select the average value at the 5th second as I_0 . After the pulse signal is applied, the average value of the 40th second is selected as I , and the pulse signals are applied at the same time. For excitatory synapses, the gain was maximized when V_{bg} base was -3 V and pulse was -4 V (pulse duration of 10 ms, interval of 200 ms), as shown in Figure 2(b) (no synaptic excitability of the h-BN/MoS₂/h-BN control devices under the same V_{bg} base and pulse conditions, see Figure S10d in Supplementary Materials). For inhibitory synapses, excitatory spike stimulation was first performed, and then fixed base, incremental V_{bg} pulse was applied, and gain and weight changes were reduced, that is, the depression effect gradually strengthened, and 8 V was selected as the inhibitory spike (duration of 10 ms, interval of 200 ms), as shown in Figure 2(c) (no synaptic inhibition of the h-BN/MoS₂/h-BN control devices under the same V_{bg} base and pulse conditions, see Figure S10e in Supplementary Materials). Figure 2(d) shows the frequency plasticity of inhibitory synapses with fixed duration of 10 ms and number of 10, and the gain gradually decreases as the frequency increases. Figure 2(e) depicts postsynaptic current characteristics under 30 cumulative excitatory and inhibitory spiking stimulations (duration of 10 ms, interval of 200 ms), which exhibits long-term potentiation and inhibition under electrical mode (the h-BN/MoS₂/h-BN control devices have no LTP and LTD characteristics under the same V_{bg} base and pulse, see Figure S10f in Supplementary Materials). Furthermore, Figure 2(f) shows extracted PSC from excitatory and inhibitory spikes, where electrical potentiation and inhibition are clearly observed. The number-dependent facilitation and depression under electrical stimulation are shown in Figure S4 in Supplementary Materials. The electrical potentiation and inhibition effects under electrical stimulation are attributed to the charges trapping and detrapping at the MoS₂-AlO_x interfaces. The statistical distribution of the maximum value of the excitatory index indicates that the excitatory index of most devices can reach 500-700% (see the statistics of 80 devices in Figure S11b in Supplementary Materials). Under forward bias (V_{bg} pulse of 8 V), the oxygen vacancy trapping states in AlO_x move toward the channel, trapping the electrons in MoS₂, causing channel current to decrease, corresponding to synaptic inhibition. While under reverse bias (V_{bg} pulse of -4 V), oxygen ions in AlO_x move toward MoS₂, and the oxygen vacancy trapping states release trapped electrons, resulting in increased channel current, which corresponds to synaptic potentiation (see Figure S5, physical mechanism under electrical stimulation in Supplementary Materials).

The realization of the association learning is of great significance for neuromorphic engineering. Pavlov's dog classical conditioning experiment is a typical associative learning experiment in physiology [56–58]. In Pavlov's dog experiment, food is called unconditional stimulation (US), while the bell and salivation are called neutral stimulation (NS) and unconditional response (UR), respectively. Food can cause salivation, while bell ringing alone does not cause salivation. Combining the bell with food, that is, after the bell

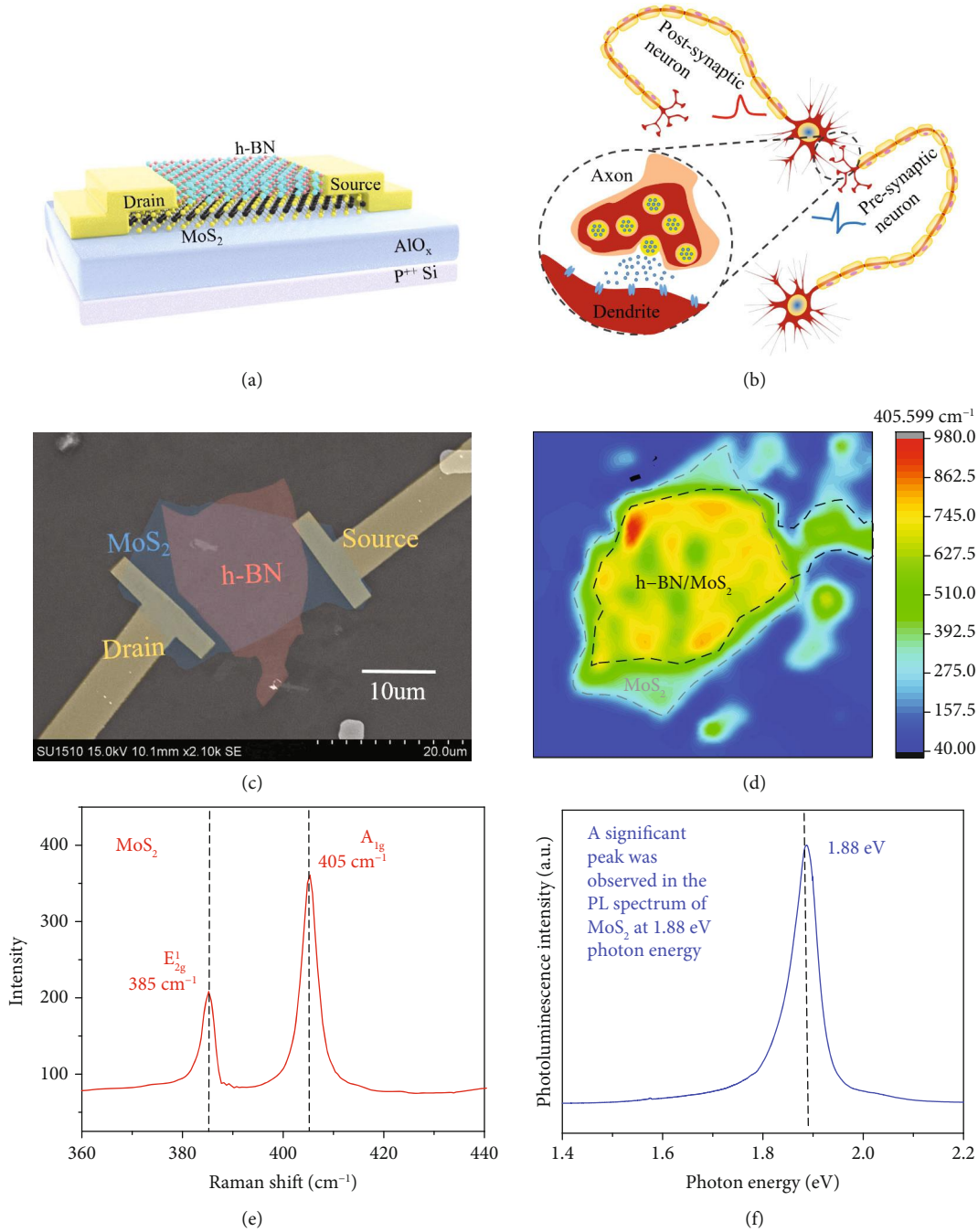


FIGURE 1: The h-BN-encapsulated MoS₂ synaptic transistor for neuromorphic engineering. (a) Schematic of h-BN-encapsulated MoS₂ synaptic transistor. (b) Schematic diagram of biological neurons and synapses as a bridge of neuronal connections. (c) False-color SEM image of h-BN-encapsulated MoS₂ synaptic transistor. (d) The Raman mapping of h-BN-encapsulated MoS₂ synaptic transistor at 405 cm⁻¹, where the black and gray dashed areas represent the h-BN/MoS₂ overlap region and channel MoS₂, respectively. (e) Raman shift of the MoS₂ characteristic peak is 385,405 cm⁻¹. (f) A significant peak was observed in the PL spectrum of MoS₂ at 1.88 eV photon energy, which is consistent with the band gap of multilayer MoS₂.

rings, the dog is fed with food, also causes salivation [57, 59]. Pavlov’s dog classical conditioning experiment can be simulated on the proposed h-BN-encapsulated MoS₂ synaptic transistor by efficient electrical modulation, as shown in Figure 3. V_{bg} (base, pulse) of (-5, -4 V) applied to the presynaptic gate is considered to be “bell” (NS), and V_{bg} (base, pulse) of (-3, -4 V) is considered “food” (US). The postsynap-

tic source drain channel current acts as synaptic weight, and the synaptic weight of 20 nA is defined as the threshold for the “salivation” response (UR). After a single training, only the “bell” ringing does not cause salivation, but after repeated training, the “bell” ringing can also cause “salivation,” which shows the same effect as feeding “food.” At this point, an association is established between “bell” and “food,” and

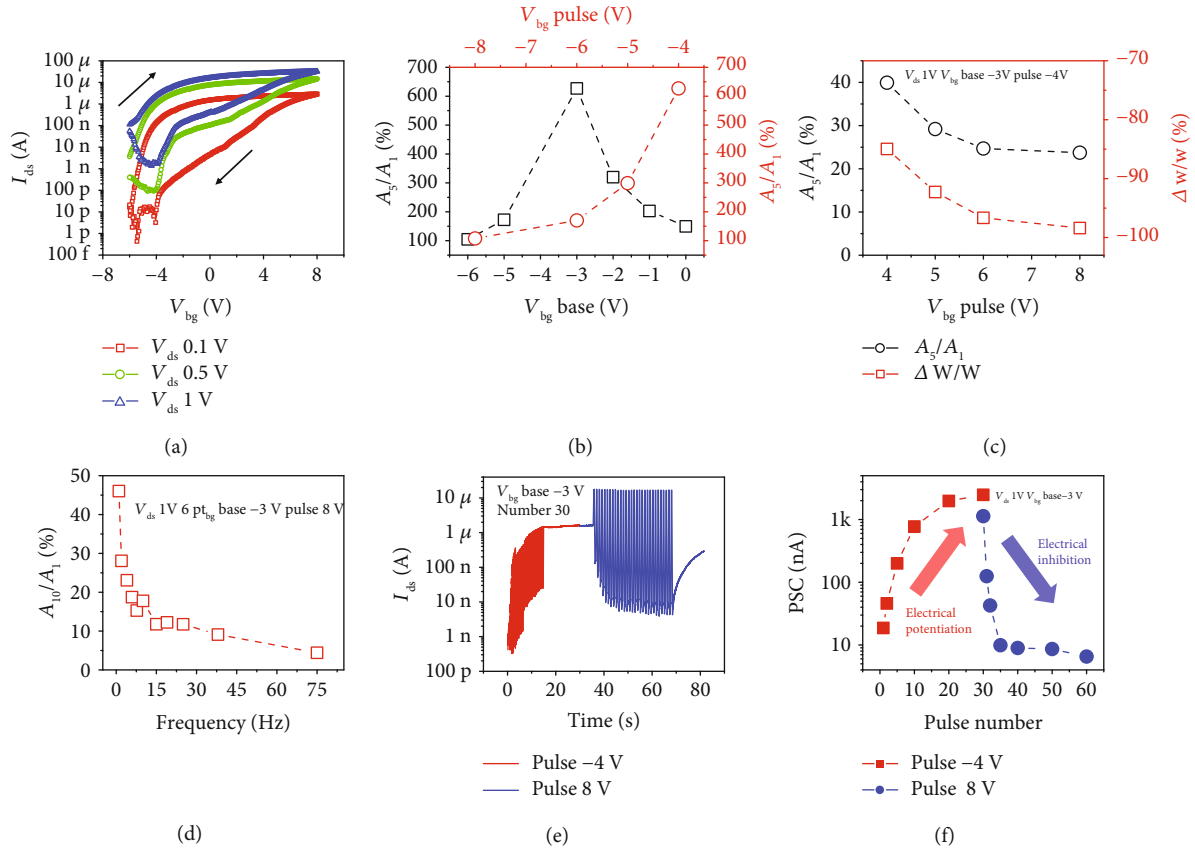


FIGURE 2: Characteristics of h-BN-encapsulated MoS₂ synaptic transistor under electrical stimulation. (a) Transfer curve under different V_{ds} . (b) Selecting the optimal base and pulse for the excitatory synapse by gain, when base of -3 V and pulse of -4 V, the maximum gain is obtained. (c) Selecting the optimal pulse of inhibitory synapse by gain and long-term synaptic weight change, the maximum inhibition effect and weight change are obtained when pulse is 8 V. (d) Frequency plasticity of inhibitory synapses, and the gain gradually decreases as the frequency increases. (e) Accumulation of postsynaptic current characteristics under 30 excitatory and inhibitory pulse stimulations. (f) Postsynaptic current characteristics as a function of progressive excitatory and inhibitory pulse stimulation numbers, showing long-term potentiation and inhibition effects.

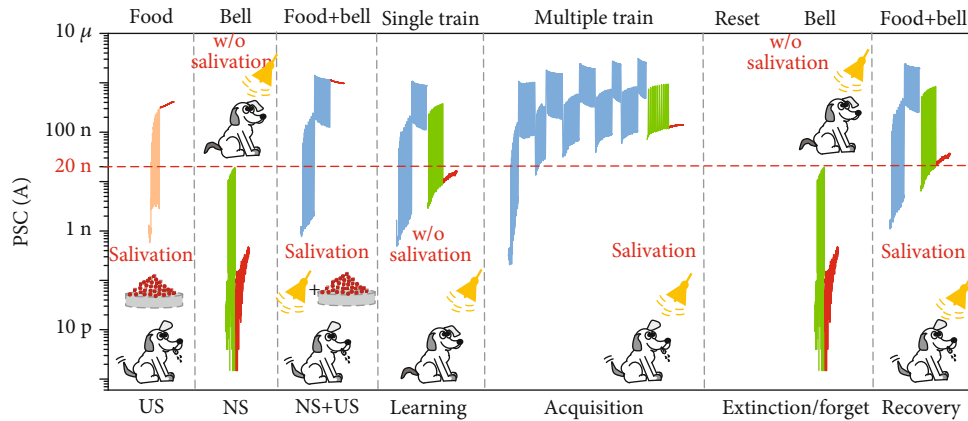


FIGURE 3: Pavlov's dog classical conditioning experiment implemented by h-BN-encapsulated MoS₂ synaptic transistor. Pavlov's dog classical conditioning experiments can be simulated on the proposed h-BN-encapsulated MoS₂ synaptic transistor by efficient electrical modulation. V_{bg} (base, pulse) of (-5, -4 V) applied to the presynaptic gate is considered to be "bell" (NS), and V_{bg} (base, pulse) of (-3, -4 V) is considered "food" (US). The postsynaptic source drain channel current acts as synaptic weight, and the synaptic weight of 20 nA is defined as the threshold for the "salivation" response.

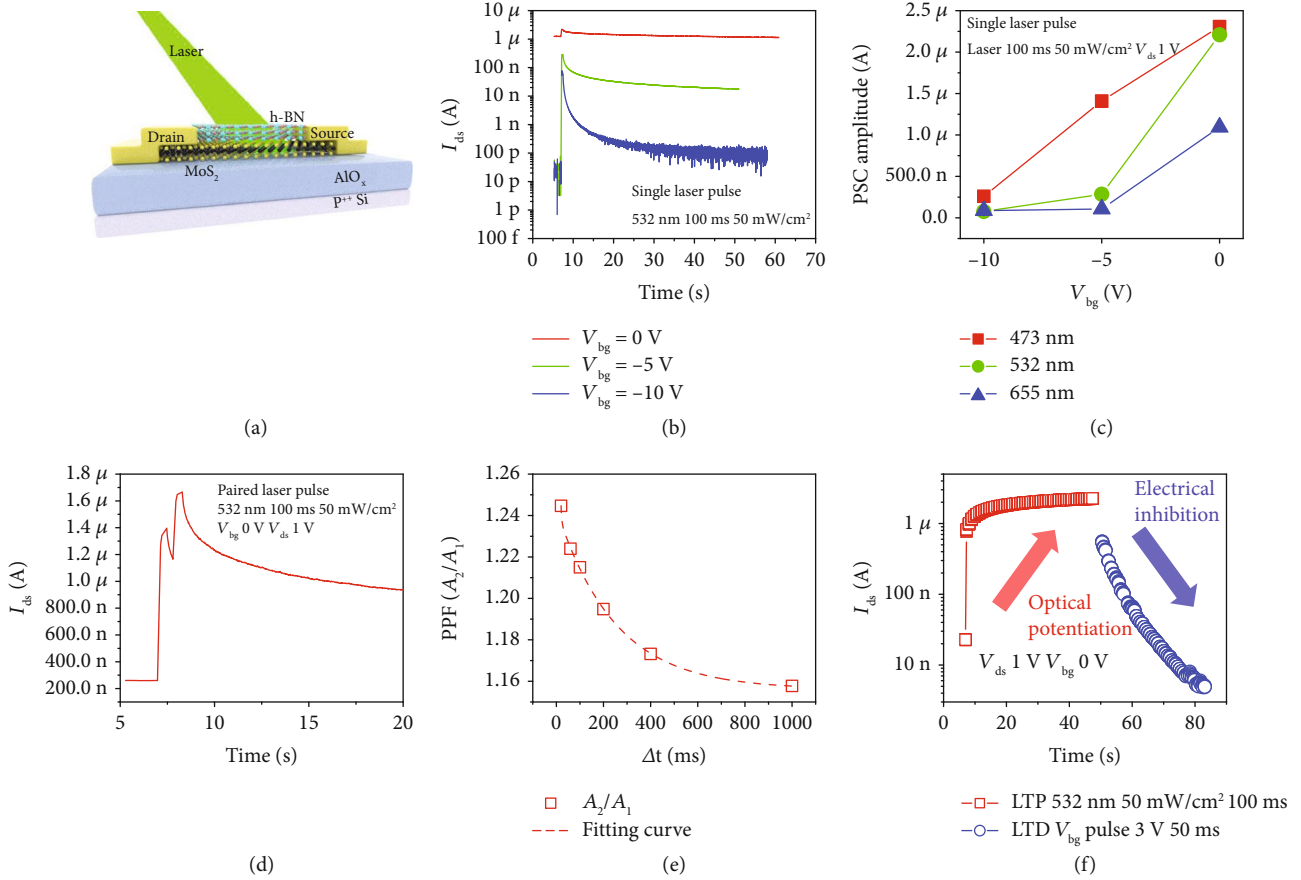


FIGURE 4: Basic synaptic characteristics of h-BN-encapsulated MoS₂ transistor under optical stimulation. (a) Schematic diagram of h-BN-encapsulated MoS₂ synaptic transistor under optical stimulus. (b) Single-laser pulse characteristics under different V_{bg} (0, -5, -10 V). (c) Variation of postsynaptic current amplitude under different V_{bg} (0, -5, -10 V) and single-laser pulses of different wavelengths (473, 532, 655 nm). (d) Typical paired laser pulse facilitation characteristics. (e) PPF characteristics as a function of paired laser pulse intervals. (f) Postsynaptic current characteristics as a function of excitatory laser pulses and inhibitory electrical pulse stimulation, which also shows long-term potentiation and depression.

the corresponding NS “bell” is converted to conditional stimulation (CS), causing a conditional response (CR) that triggers “salivation” similar to US, which is called acquisition. After a long time or reset operation, “salivation” no longer occurs when there is only CS, which means that the association between CS and US is extinct/forgotten. However, after training again, “salivation” occurs again when the “bell” rings only, that is, the association is recovered. In addition, we found that due to the existence of acquisition, the current of single training after recovery is significantly higher than the previous single training, which has exceeded the threshold and “salivation” occurs.

In addition to electrical modulation, optical spikes also enable efficient regulation of our h-BN-encapsulated MoS₂ synaptic transistor, which uses laser pulses as the photogate to adjust the channel conductance (synaptic weight), as shown in Figure 4(a). Figure 4(b) shows the single-laser pulse characteristics (532 nm, duration of 100 ms, power of 50 mW/cm²) of the synaptic transistor at V_{bg} of 0, -5, and -10 V, which significantly affect the reference current (the single-laser pulse characteristics of our synaptic transistor at 473,655 nm and the single-laser pulse current ver-

sus time at three wavelengths with V_{ds} of 1 V are detailed in Figure S6 in Supplementary Materials). Besides, variation of postsynaptic current amplitude under different V_{bg} (0, -5, -10 V) and single-laser pulses with different wavelengths (473, 532, 655 nm) is shown in Figure 4(c). We found that the PSC amplitude increases significantly with V_{bg} , where different wavelengths have little effect on the PSC amplitude (both of μA), which may be due to the excitation of the h-BN-encapsulated MoS₂ synaptic transistor at each wavelength, resulting in photocarrier accumulation in the channel. Specifically, photogenerated carriers (electron-hole pairs) are generated and separated in the top h-BN under laser duration, in which photogenerated electrons are transferred to MoS₂, resulting in an increase in channel current. With the cumulative number of laser pulses, the electrons in MoS₂ increase continuously, and the channel current appears to be nonvolatile, corresponding to the LTP behavior of neural synapses (see the physical mechanism under optical stimulation in Figure S9 in Supplementary Materials). Moreover, paired pulse facilitation (PPF) is a dynamic increase in neurotransmitter release that is thought to be critical in biosynaptic function simulations

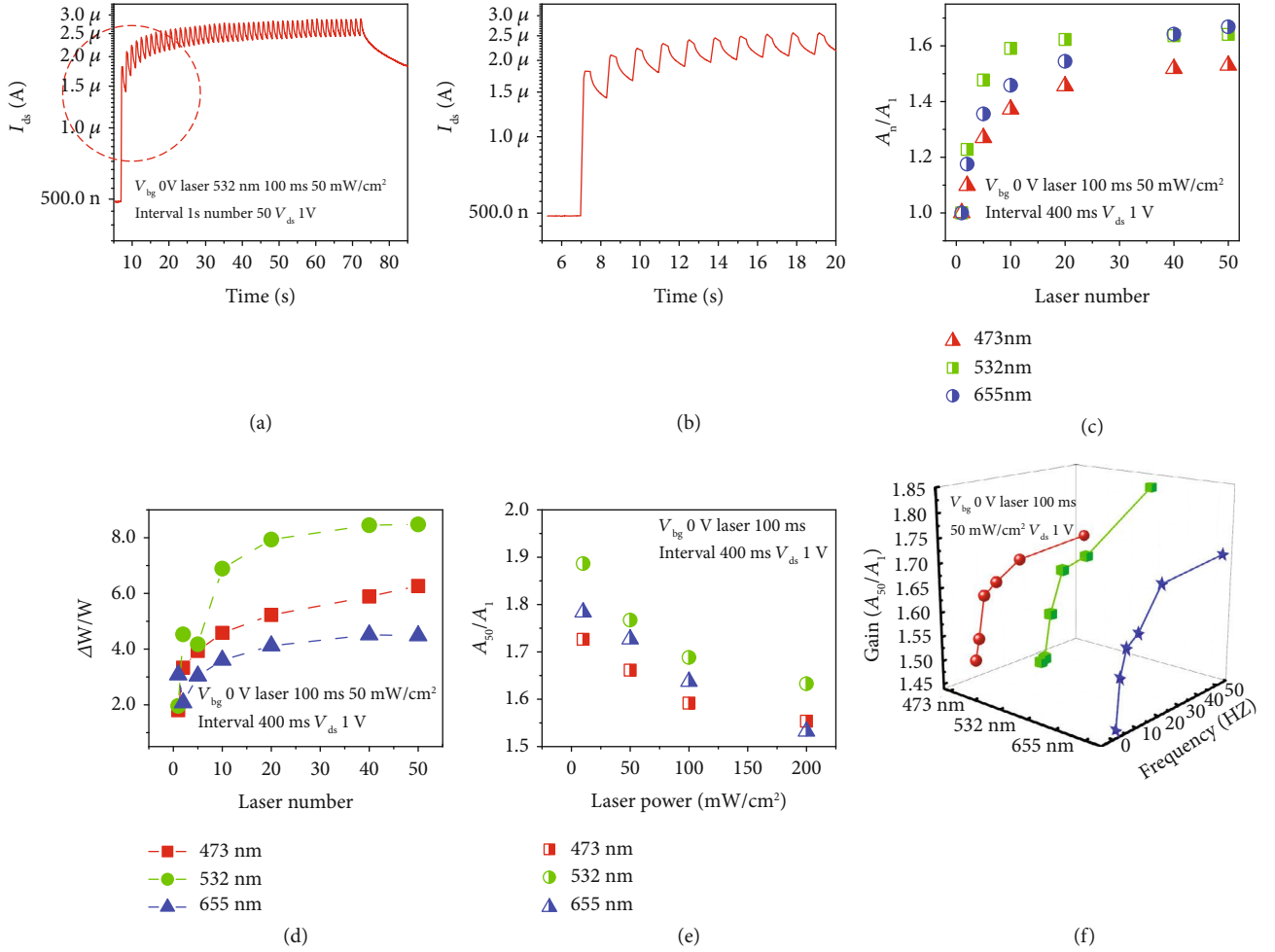


FIGURE 5: Optical neural plasticity of h-BN-encapsulated MoS₂ synaptic transistor. (a) Typical long-term potentiation of h-BN-encapsulated MoS₂ synaptic transistor under optical stimulation. (b) Magnification of the dotted circle area in (a). (c) Gain variation of different wavelengths (473, 532, 655 nm) and pulse numbers under laser stimulation. (d) Long-term synaptic weight changes at different wavelengths (473, 532, 655 nm) and pulse numbers under laser stimulation. (e) Gain variation of different wavelengths and laser powers under optical modulation. (f) Gain as a function of laser wavelength and frequency in optical modulation mode.

[60], where presynaptic-induced EPSC amplitude decreases with increasing two consecutive pulse intervals (Δt). Figure 4(d) describes the postsynaptic current response when a pair of consecutive laser pulses (532 nm, duration of 100 ms, 50 mW/cm² of power, V_{bg} and V_{ds} are 0 and 1 V) is applied. For small Δt , the postsynaptic current is further enhanced, resulting in $A_2 > A_1$, corresponding to typical synaptic PPF characteristics. Figure 4(e) exhibits the PPF index A_2/A_1 as a function of the interval time (Δt), where the red dashed line represents the fitting curve of the double exponential decay function (Equation (1)) [61]. C_1 and C_2 are the initial magnitudes of the fast and slow phases, and t_1 and t_2 are the characteristic relaxation times of the phases. For our h-BN-encapsulated MoS₂ synaptic transistor, t_1 and t_2 are about 3.0 and 247.4 ms, respectively, which is faster than in most previous work and is consistent with the relaxation time in biological synapses [16, 20, 62–65]. Moreover, we demonstrate long-term synaptic potentiation and inhibition effects under photoelectric modulation with V_{bg} and V_{ds} of 0 and 1 V, i.e., implementing optical

potentiation (532 nm, laser duration 100 ms, power 50 mW/cm²) and electrical inhibition (V_{bg} pulse 3 V, duration 50 ms) behaviors in sequence, as shown in Figure 4(f). The optimal V_{bg} pulses for inhibition under optical stimulation are explored in Figure S7 in Supplementary Materials, and 50 laser-stimulated LTP, followed by 50 electrical stimulation LTD characteristics, are shown in Figure S8 of Supplementary Materials, respectively.

$$\text{PPF}\left(\frac{A_2}{A_1}\right) = C_1 * \exp\left(\frac{-\Delta t}{t_1}\right) + C_2 * \exp\left(\frac{-\Delta t}{t_2}\right) + C_0. \quad (1)$$

Subsequently, we demonstrate the optical neural plasticity of the h-BN-encapsulated MoS₂ synaptic transistor. Figure 5(a) exhibits a typical synaptic LTP of our h-BN-encapsulated MoS₂ synaptic transistor under optical stimulation (532 nm, laser duration and intervals

are 100 ms and 1 s, power of 50 mW/cm², laser number of 50, V_{bg} and V_{ds} are 0 and 1 V), and Figure 5(b) is an enlargement of the dotted circle region in Figure 5(a). Gain (A_n/A_1) variation of different wavelengths (473, 532, 655 nm) and pulse numbers under laser stimulation (532 nm, laser duration and interval are 100 and 400 ms, power of 50 mW/cm², V_{bg} and V_{ds} are 0 and 1 V) are demonstrated in Figure 5(c), which accumulates the laser pulse numbers, and the gains under three wavelength stimuli gradually increase and tend to saturate. Besides, we demonstrate that with the increase of the laser spiking number, the long-term synaptic weight changes at different wavelengths also gradually increase, indicating the synaptic connections are strengthened, as shown in Figure 5(d). And we found that the $\Delta W/W$ induced by the 532 nm laser spike is the largest, that is, the strongest synaptic connection strength, and the weakest was at 655 nm, which may be attributed to the larger the wavelength, the smaller the energy under the same conditions, and the fewer photogenerated carriers are generated, resulting in the weakest connection strength. However, 532 nm may more easily excite our h-BN-encapsulated MoS₂ synaptic transistor than 473 nm, by concentrating more photogenerated carriers. Figure 5(e) shows the gain (A_{50}/A_1) variation of different wavelengths and laser powers under optical modulation (laser duration and interval are 100 and 400 ms, V_{bg} and V_{ds} are 0 and 1 V). Abnormally, as the laser power increases, the synaptic gain decreases, which may be attributed to the incremental power intensity causing slight damage to the channel material and degradation of performance. Finally, we also demonstrate the synaptic gain as a function of wavelength and laser frequency (1-50 Hz, duration of 100 ms, power of 50 mW/cm², V_{bg} and V_{ds} are 0 and 1 V), which increases with frequency and has a maximum at 50 Hz, as shown in Figure 5(f). PSC, PPF, gain, and $\Delta W/W$ tuning all demonstrate the flexibility and diversity of synaptic plasticity in our h-BN-encapsulated MoS₂ synaptic transistor. Besides, comparing the performance of h-BN-encapsulated MoS₂ artificial synapse with other 2D-based artificial synaptic devices, including organic and inorganic materials (such as PEDOT:PSS, CsPbBr₃, Pentacene, EMIM-TFSI, PVA, MoS₂, WSe₂, graphene, h-BN, and BP) demonstrates the superiority of our devices (see Table S1 in Supplementary Materials). The acceptable switching power consumption is estimated to be 80 pJ per spike, which is two orders of magnitude lower than the traditional CMOS [66] and even down to femtojoule when the V_{ds} is 0.1 V, close to the human brain [16]. The h-BN-encapsulated MoS₂ artificial synaptic transistor provides a novel paradigm for neuromorphic engineering based on 2D materials.

3. Discussion

In conclusion, our breakthrough, efficient, photoelectrical tunable, diverse h-BN-encapsulated MoS₂ synaptic transistor demonstrates basic synaptic functions including EPSC, PPF, LTP, LTD, synaptic gain, frequency, and weight plasticity. In addition, under electrical modulation, we successfully simulated the Pavlov classical conditioning

experiment and realized the associated learning function. It is worth mentioning that due to the h-BN encapsulation, our devices have superior environmental stability. Our synaptic transistor provides an unparalleled perspective on novel 2D material-based neuromorphic engineering and brain-like computing.

4. Materials and Methods

4.1. Preparation of the h-BN-Encapsulated MoS₂ Synaptic Transistor. We fabricated the h-BN-encapsulated MoS₂ synaptic transistor on an AlO_x/Si substrate, which simulates synaptic behavior by photoelectric stimulation, as shown in Figures 1(a) and 1(b). Firstly, two-dimensional layered h-BN and MoS₂ were prepared by mechanical exfoliation, and their thicknesses were determined by an atomic force microscope (AFM) to be about 7 and 1.7 nm, as shown in Figure S2a. The h-BN was placed on top of the MoS₂ by wet transfer using polyvinyl alcohol (PVA) as a sacrificial layer to construct an h-BN/MoS₂ heterojunction and depositing the 30 nm source-drain electrodes by electron beam evaporation (EBE) to form the synaptic transistor. The detailed manufacturing process of the h-BN-encapsulated MoS₂ synaptic transistor is shown in Figure S1.

4.2. Device Characterization and Measurement. The surface morphology of our device was characterized by scanning electron microscopy (SEM) and atomic force microscopy (AFM), as shown in Figure 1(c) and Figure S2a, respectively, showing a typical channel width of 10 μ m, a length of 15 μ m, and the thickness of the MoS₂; h-BN was approximately 1.7 and 7 nm. Besides, the 2D layered material was characterized by Raman and PL spectroscopy, as shown in Figures 1(e) and 1(f) and Figure S2b. MoS₂ shows two strong peaks near 385 and 405 cm⁻¹, corresponding to the in-plane (E_{2g}) and vertical (A_{1g}) vibration models. The Raman spectrum of h-BN reveals a peak near 1366 cm⁻¹ and also corresponds to the in-plane (E_{2g}) vibration model. The Raman mapping of h-BN-encapsulated MoS₂ synaptic transistor at 405 cm⁻¹ is shown in Figure 1(d), the channel MoS₂ exhibits intense intensity, and the h-BN/MoS₂ overlap region is more strongly correlated with h-BN encapsulation, where the black and gray dashed areas represent the h-BN/MoS₂ overlap region and channel MoS₂, respectively. A distinct peak was observed in the PL spectrum of MoS₂ at 1.88 eV photon energy, which is consistent with the band gap of multilayer MoS₂. All electrical measurements of our device were performed on the cascade probe station and Keithley 4200A semiconductor analyzer, and optical measurements were performed on the TTL/analog-modulated multiwavelength (655, 532, 473 nm) laser system.

Conflicts of Interest

The authors declare no conflict of interest.

Authors' Contributions

S. Wang designed and conducted the experiments; P. Zhou and D.W. Zhang conceived the idea; Y. Shan and S. Wu performed optical characterization of materials; X. Hou and L. Liu provided assistance with mechanism analysis and discussion.

Acknowledgments

This work was supported by the National Natural Science Foundation of China (61622401, 61851402, and 61734003), the National Key Research and Development Program (2017YFB0405600), the Shanghai Education Development Foundation, and the Shanghai Municipal Education Commission Shuguang Program (18SG01). P.Z. also acknowledges support from the Shanghai Municipal Science and Technology Commission (grant no. 18JC1410300).

Supplementary Materials

Figure S1: fabrication process scheme of h-BN-encapsulated MoS₂ synaptic transistors. It is worth mentioning that it is necessary to grow a 1 nm Al seed layer and naturally oxidize for 24 hours before depositing 30 nm Al₂O₃ as a back gate dielectric by ALD [1–3]. Figure S2: AFM image of synaptic transistor and Raman shift characterization of h-BN. (a) The AFM image of the MoS₂ synapse transistor in h-BN package, in which the MoS₂ and h-BN heights are 1.7 and 7 nm, respectively. (b) Raman shift of the h-BN characteristic peak is 1366 cm⁻¹. Figure S3: output characteristics and stability of h-BN-encapsulated MoS₂ synaptic transistors. (a) I_{ds} - V_{ds} curves and V_{bg} from -5 to 5 V in steps of 2.5 V. (b) h-BN-encapsulated MoS₂ synaptic transistors with good time and operating stability [4–7]. Figure S4: number-dependent facilitation and depression under electrical stimulation. (a) Excitatory PSC and gain under different electrical pulse numbers. (b) PSC and inhibitory ratio under different electrical pulse numbers. Figure S5: physical mechanism under electrical stimulation. (a) Under forward bias, the oxygen vacancy trapping states in AlOx move toward the channel, trapping the electrons in MoS₂, causing channel current to decrease. (b) Under reverse bias, oxygen ions in AlOx move toward MoS₂, and the oxygen vacancy trapping states release trapped electrons, resulting in increased channel current [8–10]. Figure S6: single pulse characteristics of h-BN-encapsulated MoS₂ synaptic transistors under different V_{bg} and wavelength lasers. (a) Characteristics of different V_{bg} (0, -5, -10 V) under a single 473 nm laser pulse. (b) Characteristics of different V_{bg} under a single 655 nm laser pulse. (c) Characteristics of single-laser pulses of different wavelengths under V_{bg} 0 V. Figure S7: optimal V_{bg} pulse for inhibition under optical stimulation. (a) 2 V of V_{bg} pulse. (b) 3 V of V_{bg} pulse. (c) 4 V of V_{bg} pulse. (d) 6 V of V_{bg} pulse. Figure S8: LTP and LTD behaviors under optical/electrical stimulation. (a) LTP behavior under 50 laser pulses. (b) Subsequent LTD behavior for 50 electrical pulses. Figure S9: physical mechanism under optical stimulation. (a) Photogenerated carriers (electron-hole pairs)

are generated and separated in the top h-BN under laser duration, in which photogenerated electrons are transferred to MoS₂, resulting in an increase in channel current. (b) With the cumulative number of laser pulses, the electrons in MoS₂ increase continuously, and the channel current appears to be nonvolatile, that is, LTP behavior [11]. Figure S10: characteristics of the control devices: h-BN/MoS₂/h-BN structure. (a) Schematic diagram of the control devices. (b) Micrograph of a typical control device. (c) Transfer curves of the control devices. (d) No synaptic excitability of the control devices under the same V_{bg} base and pulse conditions. (e) No synaptic inhibition of the control devices under the same V_{bg} base and pulse conditions. (f) Predictably, the control devices have no LTP and LTD characteristics under the same V_{bg} base and pulse. Figure S11: memory window and excitatory index statistics for 80 h-BN-encapsulated MoS₂ synaptic transistor. (a) The statistical distribution of the maximum value of the memory window (mean = 2.36, SD = 0.78), showing that the memory window is 2~3 V in most devices. (b) The excitability index of most devices can reach 500~700% (mean = 540.69, SD = 142.06). Table S1: comparison of 2D-based synaptic device performance, including device geometry, operating modes, electrical/optical tuning, excitatory index, long-term weight change, and power consumption. (*Supplementary Materials*)

References

- [1] J. Von Neumann, "First draft of a report on the EDVAC," *IEEE Annals of the History of Computing*, vol. 15, no. 4, pp. 27–75, 1993.
- [2] J. Backus, "Can programming be liberated from the von Neumann style? A functional style and its algebra of programs," *Communications of the ACM*, vol. 21, no. 8, pp. 613–641, 2007.
- [3] C. D. Wright, P. Hosseini, and J. A. V. Diosdado, "Beyond von-Neumann computing with nanoscale phase-change memory devices," *Advanced Functional Materials*, vol. 23, no. 18, pp. 2248–2254, 2013.
- [4] G. Indiveri and S.-C. Liu, "Memory and information processing in neuromorphic systems," *Proceedings of the IEEE*, vol. 103, no. 8, pp. 1379–1397, 2015.
- [5] R. A. Nawrocki, R. M. Voyles, and S. E. Shaheen, "A mini review of neuromorphic architectures and implementations," *IEEE Transactions on Electron Devices*, vol. 63, no. 10, pp. 3819–3829, 2016.
- [6] J. W. Dawson Jr., "The essential Turing: seminal writings in computing, logic, philosophy, artificial intelligence, and artificial life plus the secrets of enigma, by Alan M. Turing (author) and B. Jack Copeland (editor)," *The Review of Modern Logic*, vol. 10, no. 3-4, pp. 179–181, 2007.
- [7] C. Mead, "Neuromorphic electronic systems," *Proceedings of the IEEE*, vol. 78, no. 10, pp. 1629–1636, 1990.
- [8] N. K. Upadhyay, S. Joshi, and J. J. Yang, "Synaptic electronics and neuromorphic computing," *Science China Information Sciences*, vol. 59, no. 6, article 061404, 2016.
- [9] V. M. Ho, J.-A. Lee, and K. C. Martin, "The cell biology of synaptic plasticity," *Science*, vol. 334, no. 6056, pp. 623–628, 2011.

- [10] R. Yang, H.-M. Huang, Q.-H. Hong et al., "Synaptic suppression triplet-STDP learning rule realized in second-order memristors," *Advanced Functional Materials*, vol. 28, no. 5, article 1704455, 2018.
- [11] C. J. Wan, L. Q. Zhu, Y. H. Liu et al., "Proton-Conducting Graphene Oxide-Coupled Neuron Transistors for Brain-Inspired Cognitive Systems," *Advanced Materials*, vol. 28, no. 18, pp. 3557–3563, 2016.
- [12] Y. M. Fu, C. J. Wan, L. Q. Zhu, H. Xiao, X. D. Chen, and Q. Wan, "Hodgkin-Huxley artificial synaptic membrane based on protonic/electronic hybrid neuromorphic transistors," *Advanced Biosystems*, vol. 2, no. 2, article 1700198, 2018.
- [13] C. J. Wan, Y. H. Liu, P. Feng et al., "Flexible metal oxide/graphene oxide hybrid neuromorphic transistors on flexible conducting graphene substrates," *Advanced Materials*, vol. 28, no. 28, pp. 5878–5885, 2016.
- [14] Y. H. Liu, L. Q. Zhu, P. Feng, Y. Shi, and Q. Wan, "Freestanding artificial synapses based on laterally proton-coupled transistors on chitosan membranes," *Advanced Materials*, vol. 27, no. 37, pp. 5599–5604, 2015.
- [15] X. Zhu, D. Li, X. Liang, and W. D. Lu, "Ionic modulation and ionic coupling effects in MoS₂ devices for neuromorphic computing," *Nature Materials*, vol. 18, no. 2, pp. 141–148, 2019.
- [16] Y. van de Burgt, E. Lubberman, E. J. Fuller et al., "A non-volatile organic electrochemical device as a low-voltage artificial synapse for neuromorphic computing," *Nature Materials*, vol. 16, no. 4, pp. 414–418, 2017.
- [17] R. A. John, F. Liu, N. A. Chien et al., "Synergistic gating of electro-iono-photoactive 2D chalcogenide neuristors: coexistence of Hebbian and homeostatic synaptic metaplasticity," *Advanced Materials*, vol. 30, no. 25, article 1800220, 2018.
- [18] J. Zhu, Y. Yang, R. Jia et al., "Ion gated synaptic transistors based on 2D van der Waals crystals with tunable diffusive dynamics," *Advanced Materials*, vol. 30, no. 21, article 1800195, 2018.
- [19] J.-T. Yang, C. Ge, J.-Y. Du et al., "Artificial synapses emulated by an electrolyte-gated tungsten-oxide transistor," *Advanced Materials*, vol. 30, no. 34, article 1801548, 2018.
- [20] C. S. Yang, D. S. Shang, N. Liu et al., "A synaptic transistor based on Quasi-2D molybdenum oxide," *Advanced Materials*, vol. 29, no. 27, article 1700906, 2017.
- [21] X. Yan, Y. Pei, H. Chen et al., "Self-assembled networked PbS distribution quantum dots for resistive switching and artificial synapse performance boost of memristors," *Advanced Materials*, vol. 31, no. 7, article 1805284, 2019.
- [22] S. Choi, S. H. Tan, Z. Li et al., "SiGe epitaxial memory for neuromorphic computing with reproducible high performance based on engineered dislocations," *Nature Materials*, vol. 17, no. 4, pp. 335–340, 2018.
- [23] Z. Wang, S. Joshi, S. E. Savel'ev et al., "Memristors with diffusive dynamics as synaptic emulators for neuromorphic computing," *Nature Materials*, vol. 16, no. 1, pp. 101–108, 2017.
- [24] J. H. Yoon, Z. Wang, K. M. Kim et al., "An artificial nociceptor based on a diffusive memristor," *Nature Communications*, vol. 9, no. 1, p. 417, 2018.
- [25] X. Yan, J. Zhao, S. Liu et al., "Memristor with Ag-cluster-doped TiO₂ films as artificial synapse for neuroinspired computing," *Advanced Functional Materials*, vol. 28, no. 1, article 1705320, 2018.
- [26] X. Zhang, W. Wang, Q. Liu et al., "An artificial neuron based on a threshold switching memristor," *IEEE Electron Device Letters*, vol. 39, no. 2, pp. 308–311, 2018.
- [27] X. Yan, L. Zhang, H. Chen et al., "Graphene oxide quantum dots based memristors with progressive conduction tuning for artificial synaptic learning," *Advanced Functional Materials*, vol. 28, no. 40, article 1803728, 2018.
- [28] Q. Wu, H. Wang, Q. Luo et al., "Full imitation of synaptic metaplasticity based on memristor devices," *Nanoscale*, vol. 10, no. 13, pp. 5875–5881, 2018.
- [29] X. Zhang, S. Liu, X. Zhao et al., "Emulating short-term and long-term plasticity of bio-synapse based on Cu/a-Si/Pt memristor," *IEEE Electron Device Letters*, vol. 38, no. 9, pp. 1208–1211, 2017.
- [30] A. Sebastian, T. Tuma, N. Papandreou et al., "Temporal correlation detection using computational phase-change memory," *Nature Communications*, vol. 8, no. 1, article 1115, 2017.
- [31] T. Tuma, A. Pantazi, M. Le Gallo, A. Sebastian, and E. Eleftheriou, "Stochastic phase-change neurons," *Nature Nanotechnology*, vol. 11, no. 8, pp. 693–699, 2016.
- [32] G. W. Burr, R. M. Shelby, S. Sidler et al., "Experimental demonstration and tolerancing of a large-scale neural network (165 000 synapses) using phase-change memory as the synaptic weight element," *IEEE Transactions on Electron Devices*, vol. 62, no. 11, pp. 3498–3507, 2015.
- [33] T. H. Lee, D. Loke, K. J. Huang, W. J. Wang, and S. R. Elliott, "Tailoring transient-amorphous states: towards fast and power-efficient phase-change memory and neuromorphic computing," *Advanced Materials*, vol. 26, no. 44, pp. 7493–7498, 2014.
- [34] M. Suri, O. Bichler, D. Querlioz et al., "Phase change memory as synapse for ultra-dense neuromorphic systems: application to complex visual pattern extraction," in *2011 International Electron Devices Meeting*, Washington, DC, USA, December 2011.
- [35] W. Chung, M. Si, and D. Y. Peide, "First demonstration of Ge ferroelectric nanowire FET as synaptic device for online learning in neural network with high number of conductance state and G max/G min," in *2018 IEEE International Electron Devices Meeting (IEDM)*, San Francisco, CA, USA, December 2018.
- [36] S. Boyn, J. Grollier, G. Lecerf et al., "Learning through ferroelectric domain dynamics in solid-state synapses," *Nature Communications*, vol. 8, article 14736, 2017.
- [37] M. Jerry, P.-Y. Chen, J. Zhang et al., "Ferroelectric FET analog synapse for acceleration of deep neural network training," in *2017 IEEE International Electron Devices Meeting (IEDM)*, San Francisco, CA, USA, December 2017.
- [38] S. Wang, C. Chen, Z. Yu et al., "A MoS₂/PTCDA hybrid heterojunction synapse with efficient photoelectric dual modulation and versatility," *Advanced Materials*, vol. 31, no. 3, article 1806227, 2019.
- [39] C. Liu, X. Yan, X. Song, S. Ding, D. W. Zhang, and P. Zhou, "A semi-floating gate memory based on van der Waals heterostructures for quasi-non-volatile applications," *Nature Nanotechnology*, vol. 13, no. 5, pp. 404–410, 2018.
- [40] X. Yan, D. W. Zhang, C. Liu et al., "High performance amplifier element realization via MoS₂/GaTe heterostructures," *Advanced Science*, vol. 5, no. 4, article 1700830, 2018.

- [41] S. Wang, D. W. Zhang, and P. Zhou, "Two-dimensional materials for synaptic electronics and neuromorphic systems," *Science Bulletin*, vol. 64, no. 15, pp. 1056–1066, 2019.
- [42] V. K. Sangwan, H.-S. Lee, H. Bergeron et al., "Multi-terminal memtransistors from polycrystalline monolayer molybdenum disulfide," *Nature*, vol. 554, no. 7693, pp. 500–504, 2018.
- [43] W. Huh, S. Jang, J. Y. Lee et al., "Synaptic barristor based on phase-engineered 2D heterostructures," *Advanced Materials*, vol. 30, no. 35, article 1801447, 2018.
- [44] Y. Shi, X. Liang, B. Yuan et al., "Electronic synapses made of layered two-dimensional materials," *Nature Electronics*, vol. 1, no. 8, pp. 458–465, 2018.
- [45] D. Li, B. Wu, X. Zhu et al., "MoS₂ memristors exhibiting variable switching characteristics toward biorealistic synaptic emulation," *ACS Nano*, vol. 12, no. 9, pp. 9240–9252, 2018.
- [46] Y. Wang, Z. Lv, J. Chen et al., "Photonic synapses based on inorganic perovskite quantum dots for neuromorphic computing," *Advanced Materials*, vol. 30, no. 38, article 1802883, 2018.
- [47] M. Lee, W. Lee, S. Choi et al., "Brain-inspired photonic neuromorphic devices using photodynamic amorphous oxide semiconductors and their persistent photoconductivity," *Advanced Materials*, vol. 29, no. 28, article 1700951, 2017.
- [48] Z. Cheng, C. Ríos, W. H. P. Pernice, C. D. Wright, and H. Bhaskaran, "On-chip photonic synapse," *Science Advances*, vol. 3, no. 9, article e1700160, 2017.
- [49] S. Seo, S.-H. Jo, S. Kim et al., "Artificial optic-neural synapse for colored and color-mixed pattern recognition," *Nature Communications*, vol. 9, no. 1, p. 5106, 2018.
- [50] H. Tian, X. Wang, F. Wu, Y. Yang, and T.-L. Ren, "High performance 2D perovskite/graphene optical synapses as artificial eyes," in *2018 IEEE International Electron Devices Meeting (IEDM)*, San Francisco, CA, USA, December 2018.
- [51] C. Choi, M. K. Choi, S. Liu et al., "Human eye-inspired soft optoelectronic device using high-density MoS₂-graphene curved image sensor array," *Nature Communications*, vol. 8, no. 1, p. 1664, 2017.
- [52] G.-H. Lee, X. Cui, Y. D. Kim et al., "Highly stable, dual-gated MoS₂ transistors encapsulated by hexagonal boron nitride with gate-controllable contact, resistance, and threshold voltage," *ACS Nano*, vol. 9, no. 7, pp. 7019–7026, 2015.
- [53] N. Petrone, T. Chari, I. Meric, L. Wang, K. L. Shepard, and J. Hone, "Flexible graphene field-effect transistors encapsulated in hexagonal boron nitride," *ACS Nano*, vol. 9, no. 9, pp. 8953–8959, 2015.
- [54] Y. Liu, H. Wu, H. C. Cheng et al., "Towards barrier free contact to MoS₂ using graphene electrodes," 2014, <http://arxiv.org/abs/1412.7718>.
- [55] L. Wang, Z. Chen, C. R. Dean et al., "Negligible environmental sensitivity of graphene in a hexagonal boron nitride/graphene/h-BN sandwich structure," *ACS Nano*, vol. 6, no. 10, pp. 9314–9319, 2012.
- [56] Z.-H. Tan, X.-B. Yin, R. Yang, S. B. Mi, C. L. Jia, and X. Guo, "Pavlovian conditioning demonstrated with neuromorphic memristive devices," *Scientific Reports*, vol. 7, no. 1, p. 713, 2017.
- [57] Y. Li, L. Xu, Y.-P. Zhong et al., "Associative learning with temporal contiguity in a memristive circuit for large-scale neuromorphic networks," *Advanced Electronic Materials*, vol. 1, no. 8, article 1500125, 2015.
- [58] S. Hu, Y. Liu, Z. Liu et al., "Associative memory realized by a reconfigurable memristive Hopfield neural network," *Nature Communications*, vol. 6, no. 1, p. 7522, 2015.
- [59] C. Wu, T. W. Kim, T. Guo, F. Li, D. U. Lee, and J. J. Yang, "Mimicking classical conditioning based on a single flexible memristor," *Advanced Materials*, vol. 29, no. 10, article 1602890, 2017.
- [60] D. Sarkar, J. Tao, W. Wang et al., "Mimicking Biological Synaptic Functionality with an Indium Phosphide Synaptic Device on Silicon for Scalable Neuromorphic Computing," *ACS Nano*, vol. 12, no. 2, pp. 1656–1663, 2018.
- [61] R. S. Zucker and W. G. Regehr, "Short-term synaptic plasticity," *Annual Review of Physiology*, vol. 64, no. 1, pp. 355–405, 2002.
- [62] M. T. Sharbati, Y. Du, J. Torres, N. D. Ardolino, M. Yun, and F. Xiong, "Low-power, electrochemically tunable graphene synapses for neuromorphic computing," *Advanced Materials*, vol. 30, no. 36, article 1802353, 2018.
- [63] H. K. He, R. Yang, W. Zhou et al., "Photonic potentiation and electric habituation in ultrathin memristive synapses based on monolayer MoS₂," *Small*, vol. 14, no. 15, article 1800079, 2018.
- [64] J. Jiang, J. Guo, X. Wan et al., "2D MoS₂ neuromorphic devices for brain-like computational systems," *Small*, vol. 13, no. 29, article 1700933, 2017.
- [65] A. A. Bessonov, M. N. Kirikova, D. I. Petukhov, M. Allen, T. Ryhänen, and M. J. Bailey, "Layered memristive and memcapacitive switches for printable electronics," *Nature Materials*, vol. 14, no. 2, pp. 199–204, 2015.
- [66] G. Indiveri, E. Chicca, and R. Douglas, "A VLSI array of low-power spiking neurons and bistable synapses with spike-timing dependent plasticity," *IEEE Transactions on Neural Networks*, vol. 17, no. 1, pp. 211–221, 2006.